Materials Today Bio 30 (2025) 101427

Contents lists available at ScienceDirect

Materials Today Bio

journal homepage: www.journals.elsevier.com/materials-today-bio

Multifunctional drug delivery nanoparticles for combined chemotherapy/chemodynamic/photothermal therapy against colorectal cancer through synergistic cuproptosis/ferroptosis/apoptosis

Xiuzhang Yan [a], Heshi Liu [b], Lei Guo [b], Chang Liu [b], Shichen Zhang [b], Xue Wang [b], Yixin Tang [b], Rui Zhou [b], Xin Jiang [b], Erlei Wang [c,**], Shuohui Gao [a,***], Caina Xu [b,*]

[a] Department of Gastrointestinal Colorectal Surgery, Jilin University China-Japan Union Hospital, Changchun, 130000, China
[b] College of Basic Medical Sciences, The Medical Basic Research Innovation Center of Airway Disease in North China, Key Laboratory of Pathobiology, Ministry of Education, Jilin University, Changchun, 130021, China
[c] College of Food Science and Engineering, Jilin University, Changchun, 130062, China

ARTICLE INFO

Keywords:
Colorectal cancer
Cuproptosis
Ferroptosis
MIL-100
Photothermal therapy

ABSTRACT

The use of combination therapies that employ a variety of cell death mechanisms has emerged as a promising avenue of research in the treatment of cancer. However, the optimization of therapeutic synergies when integrating different modes remains a significant challenge. To this end, we developed a multifunctional intelligent drug-carrying nanoparticle (DFMTCH NPs) based on the metal-organic framework MIL-100, loaded with doxorubicin (DOX) and disulfiram (DSF), coated with a Cu-tannic acid (Cu-TA) network and hyaluronic acid (HA), for the purpose of combined chemotherapy/chemodynamic/photothermal anti-cancer therapy. On the one hand, the DFMTCH NPs exhibited a range of therapeutic capabilities, including chemotherapy, photothermal therapy (PTT), and chemodynamic therapy (CDT), which collectively enhanced the anti-tumor efficacy of chemotherapeutic agents. In addition, DFMTCH NPs proved sensitive photoacoustic imaging (PAI) in image-guided therapy. On the other hand, DFMTCH NPs could produce reactive oxygen species (ROS) and consume glutathione (GSH) by amplifying cellular oxidative stress, while causing intracellular mitochondrial dysfunction, inducing effective cuproptosis/ferroptosis/apoptosis to inhibit tumor growth. Collectively, this work provided an innovative strategy for designing multifunctional nanoparticles for effective combination therapies to combat colorectal cancer (CRC).

1. Introduction

Colorectal cancer (CRC) has a significant impact on human health worldwide and ranking as the third most common cancer in the world [1]. The conventional treatment for patients with CRC includes surgical resection, endoscopic resection, radiotherapy, and chemotherapy [2]. Chemotherapy plays a pivotal role in eradicating residual CRC cells following local surgery for CRC [2]. However, chemotherapy for CRC faces a number of challenges, including unsatisfactory therapeutic efficacy due to tumor cells exhibiting strong drug resistance of tumor cells and the high side effects of chemotherapeutic agents [3]. Therefore, exploring synergistic anti-cancer strategies that operate through multiple anti-tumor mechanisms is necessary to improve anti-tumor efficacy and minimize the side effects of chemotherapy. In recent years, new strategies for tumor treatment, such as chemodynamic therapy (CDT) and photothermal therapy (PTT), have received widespread attention due to their high efficacy and low adverse reactions [4,5]. Among the aforementioned approaches, CDT is a novel therapeutic approach that relies on the Fenton/Fenton-like reaction, which converts hydrogen peroxide (H_2O_2) in tumor cells into highly cytotoxic hydroxyl radicals

* Corresponding author.
** Corresponding author.
*** Corresponding author.
E-mail addresses: jlbsyxz123@163.com (X. Yan), hsliu23@mails.jlu.edu.cn (H. Liu), guolei981112@163.com (L. Guo), drliuchang@jlu.edu.cn (C. Liu), zhangsc21@mails.jlu.edu.cn (S. Zhang), xuew22@mails.jlu.edu.cn (X. Wang), tangyx21@mails.jlu.edu.cn (Y. Tang), zhourui23@mails.jlu.edu.cn (R. Zhou), xinjiang@jlu.edu.cn (X. Jiang), wel@jlu.edu.cn (E. Wang), shgao@jlu.edu.cn (S. Gao), xucaina@jlu.edu.cn (C. Xu).

https://doi.org/10.1016/j.mtbio.2024.101427
Received 30 October 2024; Received in revised form 11 December 2024; Accepted 23 December 2024
Available online 29 December 2024
2590-0064/© 2024 The Authors. Published by Elsevier Ltd. This is an open access article under the CC BY-NC license (http://creativecommons.org/licenses/by-nc/4.0/).

(·OH) without the use of external energy sources [4]. This approach offers a promising way to kill cancer cells. Moreover, PTT relies on generating high temperatures through photothermal agents under near-infrared (NIR) light irradiation to physically damage malignant cells. This approach has inherent advantages, including high spatial selectivity, non-resistance, low invasiveness, and low side-effects, making it a highly promising approach for precision cancer therapy [5–7]. At present, a large number of studies have successfully applied photothermic agents to tumor treatment, and achieved good anti-tumor effect [8–10]. Additionally, some photothermal agents can also convert light absorption into ultrasound energy for guided localization by photoacoustic imaging (PAI) [11]. The combination of chemotherapy, PTT with CDT has the potential to overcome the resistance of tumor cells to apoptosis, thereby improving the outcome of tumor treatment.

In the previous study, Tsvetkov et al. identified a non-apoptotic cell death pathway induced by copper overload called cuproptosis, which is different from other widely studied programmed cell death modes such as apoptosis and has the potential to overcome the current limitations of chemotherapy [12,13]. Cuproptosis is characterized by the aggregation of lipid acylated proteins and the loss of iron-sulfur cluster proteins, resulting in proteotoxic stress and ultimately cell death [13]. Cu^{2+} has been shown to exhibit significantly higher catalytic activity over a wider pH range, however, maintaining a high concentration of copper in the cytosol for effective cuproptosis is difficult due to the insufficient concentration of free copper in cancer cells under physiological conditions [14]. In addition, ferroptosis is another type of non-apoptotic cell death accompanied by an abnormal accumulation of metal-dependent reactive oxygen species (ROS), which exacerbates the dysregulation of intracellular Reduction-Oxidation (REDOX) balance [15]. There is now ample evidence that ferroptosis is a promising therapeutic strategy for tumor suppression, primarily due to its potential to circumvent chemotherapeutic drug-based apoptosis resistance [16,17]. However, the efficacy of ferroptosis-based therapies is still limited by the suboptimal Fenton-like activity of Fe^{3+} [18]. Therefore, in order to enhance the efficacy of ferroptosis, as well as cuproptosis and CDT, doping copper ions in iron-based smart nanocarriers is a promising approach for tumor therapy. In addition to exhibiting superior Fenton-like activity, simultaneous Fe^{3+} and Cu^{2+}-based nanoplatforms have the potential to deplete glutathione (GSH) more efficiently, offering great promise for amplifying oxidative stress [19]. Therefore, the combination of Cu/Fe-mediated cuproptosis/ferroptosis would be an effective approach to maximize therapeutic efficacy through the exploitation of synergistic effects.

MIL-100, a type of nanoscale metal-organic framework (nMOF) composed of iron, has been widely used to deliver anti-tumor drugs due to its pH degradability, high porosity, and low cost [20]. In this study, MIL-100 was used to load the classic chemotherapy drugs doxorubicin (DOX) and disulfiram (DSF). Then the exterior of the drug-loaded MIL-100 was covered with a Cu-Tannic Acid (Cu-TA) network. Finally, hyaluronic acid (HA) was wrapped in the outermost layer as a shielding layer to obtain a multifunctional smart nanocarrier platform DFMTCH NPs, which combined with the chemotherapy/CDT/PTT strategy for synergistic anti-cancer treatment and achieved synergistic anti-tumor mechanism of cuproptosis/ferroptosis/apoptosis (Fig. 1). This platform exhibited several advantages over existing nanodrug delivery systems for CRC. 1) DFMTCH NPs had special nanoparticle size, which could be accumulated at tumor sites *in vivo* by the EPR effect. 2) DFMTCH NPs not only exhibited stable PAI capability, and also could be used for photothermal imaging due to their high PTT efficiency. 3) DFMTCH NPs were loaded with two chemotherapeutic drugs, DOX and DSF, and released the drugs in a pH-responsive manner, achieving precise drug release, good chemotherapy efficacy, and minimal side effects. 4) The combined use of multiple anti-tumor strategies, including chemotherapy, CDT, and PTT, had overcome tumor drug resistance and

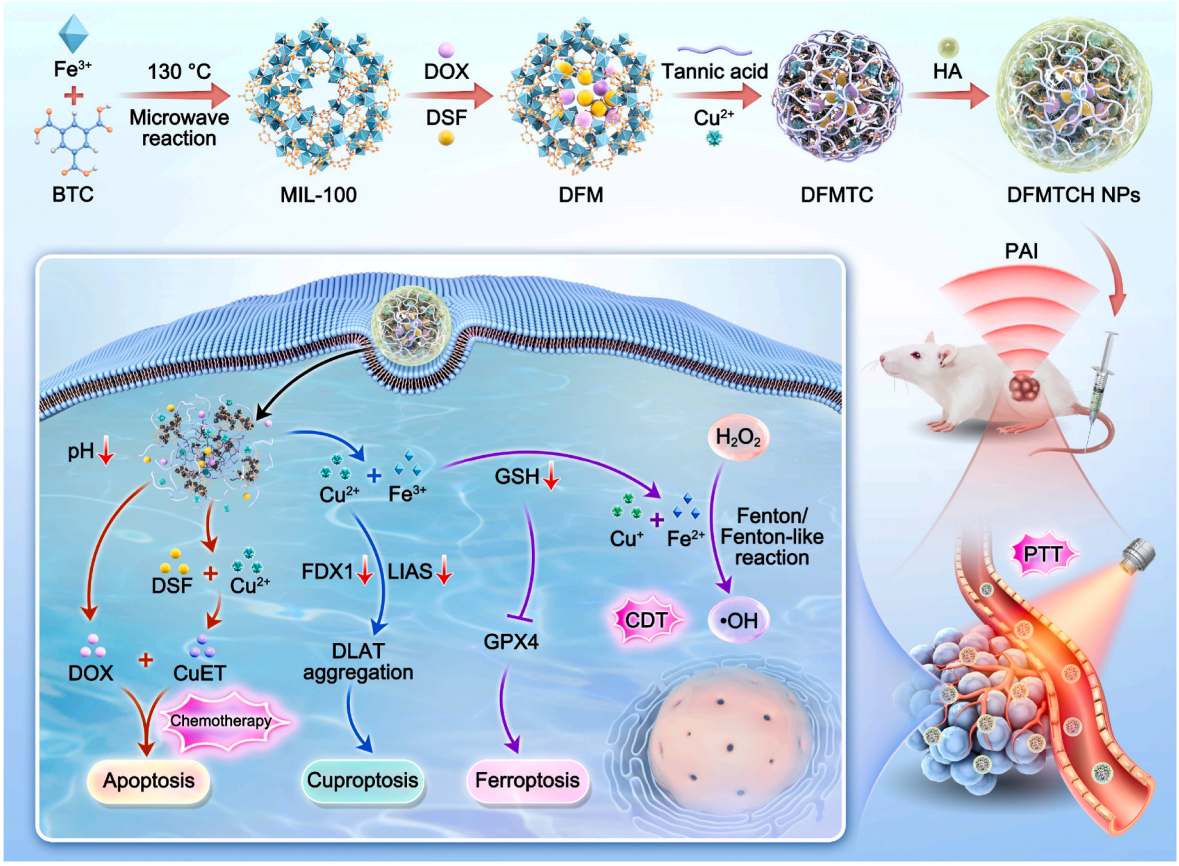

Fig. 1. Schematic representation of DFMTCH NPs synthesis and DFMTCH NPs-based cancer therapy in mice.

achieved good therapeutic effects. 5) Due to the substantial quantity of anti-tumor drugs loaded, along with the high concentration of Fe^{3+} and Cu^{2+}, DFMTCH NPs could simultaneously induce apoptosis, ferroptosis and cuproptosis, which resulted in a synergistic effect and effectively eliminated tumor cells. In conclusion, the multifunctional nanoparticles DFMTCH NPs had the potential to induce cuproptosis, ferroptosis and apoptosis by combining chemotherapy, CDT, and PTT, providing a promising therapeutic approach for effective cancer treatment and a potential strategy for the development of future CRC treatments.

1.1. Materials

1,3,5-Benzenetricarboxylic acid (BTC), $FeCl_3{\cdot}6H_2O$, $Cu(NO_3)_2{\cdot}5H_2O$, tannic acid (TA), methylene blue (MB), 5,5′-Dithio bis-(2-nitrobenzoic acid) (DTNB), DOX and DSF were obtained from Aladdin (Shanghai, China). HA was purchased from Freda (Shandong, China). Mitochondrial membrane potential test kit (JC-1), active oxygen species assay kit, GSH and GSSG assay Kit, EdU Cell Proliferation Kit with Alexa Fluor 488, Cytotoxicity Assay Kit for Animal Live & Dead Cells, Lipid Peroxidation Assay Kit with BODIPY 581/591C11, and lipid peroxidation malondialdehyde (MDA) assay kit were purchased from Beyotime Biotech (Nantong, China). Dulbecco's modified Eagle's medium (DMEM) and fetal bovine serum (FBS) were purchased from Gibco (Grand Island, USA). Glutathione peroxidation 4 (GPX4) antibody (DF6701), ferredoxin-1 (FDX1) antibody (DF7950), and lipoic acid synthase (LIAS) antibody (DF14836) were acquired from Affinity Biosciences (Jiangsu, China). Caspase-3 antibody, β-Actin antibody and lipoylated protein dihydrolipoamide S-acetyltransferase (DLAT) antibody were sourced from Proteintech (Wuhan, China).

1.2. Preparation of MIL-100 NPs

MIL-100 NPs was prepared by microwave-assisted synthesis according to a previous study [21]. First, $FeCl_3{\cdot}6H_2O$ dissolved (0.84 g) and BTC (0.27 g) in N, N-dimethylformamide (DMF) and stir thoroughly. The mixture was then placed in a microwave reactor and reacted at 130 °C for 5 min. After natural cooling, the product was centrifuged at 12,000 rpm for 20 min. The precipitate was washed 3 times with DMF to obtain MIL-100 NPs.

1.3. Preparation of DFMTCH NPs

In order to prepare DFMTCH NPs, MIL-100 NPs and DOX were fully dispersed in deionized water, and then the methanol solution of DSF in equal volume was added to the mixture, and the mixed solution was placed in a vacuum drying oven at 38 °C, 0.8 Pa, and stood for 24 h away from light. Then, the above solution was centrifuged at 12,000 rpm for 10 min, the supernatant was discarded and washed with deionized water three times to obtain DOX/DSF@MIL-100 NPs (DFM NPs).

After fully dispersing DFM NPs (1 mg) in deionized water (1 mL), added TA (pH = 8, 10 mg/mL, 50 μL) and $Cu(NO_3)_2{\cdot}5H_2O$ (10 mg/mL, 100 μL) solution, stirred for 5 min, centrifuged at 10,000 rpm for 10 min, discarded the supernatant, and washed with deionized water for 3 times, DOX/DSF@MIL-100@TA-Cu NPs (DFMTC NPs) was obtained. DFMTC NPs was suspended in deionized water, added with HA, stirred for 24 h, centrifuged again and discarded supernatant to obtain DOX/DSF@MIL-100@TA-Cu-HA (DFMTCH) NPs. The preparation methods of DOX@MIL-100@TA-Cu-HA (DMTCH) NPs, and DSF@MIL-100@TA-Cu-HA (FMTCH) NPs referred to the preparation process of DFMTCH NPs, except that only one of the drugs was introduced into the synthesis process.

1.4. Particle size and stability of DFMTCH NPs

The hydrated particle size of MIL-100 NPs, DFM NPs and DFMTCH NPs were measured by Malvern Zetasizer Lab (Malvern, UK). In addition, DFMTCH NPs was dissolved in deionized water, phosphate buffered saline (PBS) and DMEM (10 % FBS) solution, and the stability of DFMTCH NPs was evaluated by observing the changes of hydrated particle size at different times (0, 4, 8, 12, 24, 48, and 72 h, respectively).

1.5. In vitro pH response to drug release

DFMTCH NPs (4 mg) was packed into a dialysis bag (MWCO = 3.0 kDa) and then the bag was slowly stirred in a 20 mL PBS beaker with different pH values (pH = 7.4 or 5.5) at 37 °C. Then the test solution (1 mL) was collected at different time intervals (0.5, 1, 2, 4, 6, 12, 24, 48, and 72 h), and the contents of DOX and DSF released by DFMTCH NPs were determined by UV–VIS spectrophotometer. At the same time, 1.0 mL of fresh PBS of the same pH was added to the beaker.

1.6. In vitro cellular uptake

CT-26 cells were incubated with DFMTCH NPs in a 6-well plate for 2, 4, and 8 h. After staining with 4′,6-diamidino-2-phenylindole (DAPI) and washing with PBS three times, the cells were observed under a fluorescence microscope.

1.7. In vitro photothermal performance of DFMTCH NPs

First, DFMTCH NPs in different concentrations (0.5, 1.0, and 1.5 mg/mL) were prepared. In order to evaluate the photothermal performance of DFMTCH NPs, 1 mL of DFMTCH NPs with different concentrations was put into a test tube and irradiated with 808 nm laser (1, 1.5, and 2 W/cm^2) of different powers for 10 min. The temperature during irradiation was recorded with an infrared imager. In addition, the photothermal stability of DFMTCH NPs solution was also studied. After irradiating DFMTCH NPs solution (808 nm laser) for 6 min, the laser was turned off and the solution was cooled to room temperature. Five cycles were repeated to record the temperature change.

1.8. Photoacoustic imaging

First, CT-26 cells (1×10^6 cells/50 μL) were implanted into the right side of Balb/c mice to establish a tumor model. When the tumor was about 150 mm^3, a solution of DFMTCH NPs was injected intravenously into the mice. At 0, 6, 12, and 24 h after injection, the mice were anesthetized with 2 % isoflurane and then placed in a multispectral optoacoustic tomography system (MSOT scanner, iThera Medical, Germany) for multispectral process scanning. The scan results were reconstructed using a linear model and linear regression analysis was performed.

1.9. Cytotoxicity and cell viability rescue assay

The cytotoxicity of DFMTCH NPs was detected by MTT assay. Briefly, different concentrations of MIL-100 NPs, DOX, DSF, DMTCH NPs, FMTCH NPs were incubated with CT-26 cells for 24 h. 3-(4, 5-dimethylthiazole-2-yl)-2, 5-diphenyl tetrazole bromide (MTT) was used to detect cell viability at 492 nm. For PTT, different concentrations of DFMTCH NPs were incubated with CT-26 cells. After incubation for 4 h, the cells were irradiated with 808 nm laser at 1.5 W/cm^2 for 5 min, then incubated for 20 h, washed twice with cold PBS, and the cytotoxicity was determined by MTT method. Subsequently, the cells were stained with Calcein-AM (AM) and propyl iodide (PI) and observed by fluorescence microscopy.

Similarly, DFMTCH NPs (10 μg/mL) was incubated with ferroptosis inhibitors ethylene diamine tetraacetic acid (EDTA), deferoxamine mesylate (DFO), ferrostatin-1 (Fer-1), and cuproptosis inhibitor tetrathiomolybdate (TTA) with CT-26 cells for 24 h, respectively, and cell viability was measured to examine the mode of cell death induced by

DFMTCH NPs.

1.10. ROS generation and GSH-depletion ability

MB was used as a probe to monitor ROS production. A 10 μL aliquot of DFMH NPs, DFMTH NPs, or DFMTCH NPs was added to a buffer containing 10 μg/mL MB and 5 mM H_2O_2, and the mixture was then incubated at 37 °C for 30 min. Finally, the absorbance change of MB was monitored with an ultraviolet–visible spectrophotometer at 650 nm. In addition, ROS production was measured by detecting the absorbance change of MB at different DFMTCH NPs concentrations.

DTNB reacts with GSH to produce yellow products with a unique absorption peak at 410 nm [22]. To investigate the GSH consumption capacity of DFMTCH NPs, 10 μL of DFMH NPs, DFMTH NPs, and DFMTCH NPs were added to 10 mM GSH solution and buffer solution, incubated in the dark for 2 h, and then mixed with DTNB (10 μL, 100 μM). The absorption spectrum was then detected by UV–VIS spectrophotometer. Furthermore, the absorbance changes of DFMTCH NPs at different concentrations were also monitored to ascertain the extent of GSH depletion.

1.11. Colony formation assay

Cell growth and colony formation capacity were monitored using colony formation assays. CT-26 cells were seeded into a six-well plate (600 cells/well). The cells were incubated with MIL-100 NPs, free DOX, free DSF, and DFMTCH NPs in 5 % CO_2 at 37 °C. Change the medium every three days until colonies appear. The colony was fixed in 4 % polyformaldehyde for 10 min, and then stained with 1 % crystal violet at room temperature for 10 min. Colony growth was observed by counting the number of colonies.

1.12. Wound healing assay

The cell migration was studied by scratch healing *in vitro*. CT-26 cells were inoculated on a 6-well plate, and after adhesion, linear scratches were made on the cell monolayers with the tip of a 200 μL pipette. Then the cells were incubated with MIL-100 NPs, free DOX, free DSF, and DFMTCH NPs, and the scratches were observed with light microscopy at different times.

1.13. Migration assay

The migration activity of CT-26 cells was detected by Transwell migration assay. A 24-well Transwell with a pore size of 8 μm was selected for migration test. DMEM containing 10 % FBS was injected into the lower cavity, and 200 μL serum-free DMEM was injected into the upper cavity, and about 5×10^4 CT-26 cells were added. After incubation for 24 h the cells were fixed with paraformaldehyde, stained with crystal violet for 20 min, and the non-migrated cells were wiped away with a cotton swab. Finally, the cell migration was observed with an optical microscope.

1.14. Western blot analysis

CT-26 cells were inoculated in 6-well plates, then treated with different nanoparticles and incubated for 24 h. After incubation, cells were harvested and lysed for total protein extraction. Finally, standard western blot analysis was used to detect key markers such as glutathione peroxidation 4 (GPX4), lipoic acid synthase (LIAS), ferredoxin-1 (FDX1), and Caspase-3.

1.15. Intracellular ROS measurement

2′, 7′-dichlorodihydrofluorescein diacetate (DCFHDA) is used as a probe to detect reactive oxygen species (ROS) [23]. Non-fluorescent DCFHDA is oxidized by ROS to fluorescent DCF in cells. The green fluorescence signal was detected using fluorescence microscopy or CLSM. Therefore, the level of ·OH in cells could be reflected by the intensity of green fluorescence. In short, CT-26 cells were inoculated into a 24-well plate and incubated at 37 °C for 4 h with different drugs and nanoparticles. The cells were washed with PBS and then cultured in 2 mL serum-free medium containing 1 mL DCFHDA (10 μM) in the dark for 30 min ·OH production was monitored using fluorescence microscopy.

1.16. Mitochondrial membrane potential detection

The mitochondrial membrane potential was observed by JC-1 staining. CT-26 cells in 6-well plates were incubated with DFMTCH NPs. After treatment for 24 h, JC-1 was added and incubated for 30 min. Fluorescence was observed by fluorescence microscope.

1.17. LPO assay, MDA assay and intracellular GSH assay

As recommended by the manufacturer, a lipid peroxidation MDA assay kit was used to assess the relative levels of malondialdehyde in cell lysates. Cells was homogenized with MDA lysate on ice with CT-26 cells and then centrifuged (12,000 rpm, 10 min) to remove insoluble components. The sample or a mixture of standard buffer (100 μL) and 200 μL thiobarbituric acid (TBA) solution was incubated at 100 °C for 15 min to produce an MDA-TBA adduct with a proportional chromaticity (OD = 532 nm). Each sample (200 μL) was cooled to room temperature and transferred to a 96-well plate, and the absorbance was analyzed by enzyme-labeled analyzer at 532 nm. MDA concentration was calculated according to the standard curve. Similarly, intracellular GSH levels in CT-26 cells were quantified using the GSH/GSSG assay kit as per the manufacturer's instructions. Similarly, the Lipid Peroxidation Assay Kit with BODIPY 581/591C11 was used to demonstrate ferroptosis as recommended by the manufacturer to detect intracellular lipid peroxides (LPO).

1.18. Mice subcutaneous CT-26 tumor model and treatment

All animal experiments were conducted under the guidance of experimental animals established by the Animal Protection and Utilization Committee of Jilin University. All procedures were carried out in accordance with the Guidelines for Ethical Review of Laboratory Animals. CT-26 cells (1×10^6 cells) were implanted subcutaneously into the right hind leg of Balb/c mice. When the tumor volume reached 150 mm^3, CT-26 tumor-carrying mice were randomly divided into seven groups: PBS (group I), MIL-100 NPs (group II), free DOX (Group III), DMTCH NPs (group IV), FMTCH NPs (group V), DFMTCH NPs (group VI) and DFMTCH NPs + Laser (group VII). The CT-26 tumor-bearing mice were injected with the drug every 2 days through the tail vein. The tumor sites of group VII mice were irradiated with 1 W/cm^2, 808 nm laser for 10 min at 12 h after injection. The temperature inside the tumor during irradiation was recorded by an infrared imaging camera. The body weight and tumor volume of mice were accurately measured every 2 days. On day 20, all mice were euthanized and blood and major organs (heart, liver, spleen, lung, and kidney) were collected for analysis. Tumor tissue images were taken for each group, and tumors were extracted according to standard procedures for H&E staining, dUTP notch end labeling (TUNEL) staining mediated by terminal deoxynucleotide transferase, and immunohistochemistry.

DFMTCH NPs was injected into CT-26 tumor-bearing mice through the tail vein when the tumor volume reached about 200 mm^3. Then the mice were anesthetized at 2, 6, 12, 24, and 48 h, respectively. Major organs (heart, liver, spleen, lung, and kidney) and tumors were collected for fluorescence imaging using the Maestro *in vivo* imaging System (Cambridge Research & Instrumentation, Inc., USA).

1.19. Hemocompatibility test

The blood compatibility of DFMTCH NPs was determined by hemolysis test. Fresh blood from mice was centrifuged at 1500 rpm at 4 °C for 5 min to separate red blood cells from plasma, and then washed with sterile PBS for 3 times. The red blood cell precipitate was mixed with normal saline to obtain a 2 % red blood cell suspension. Different concentrations of DFMTCH NPs were dissolved in 200 μL normal saline and then mixed with 200 μL red cell suspension. After incubation at 37 °C for 4 h, the mixture was centrifuged (3500 rpm, 5 min), and the absorption of the supernatant at 540 nm was monitored with an enzyme label.

2. Results and discussion

2.1. Synthesis and characterization

The process for preparing MIL-100 NPs and DFMTCH NPs was illustrated in Fig. 2A. The first step involved the preparing MIL-100 NPs using an improved microwave-assisted reaction. Subsequently, DOX and DSF were loaded into the MIL-100 NPs to produce DFM NPs. Then, the nanoparticles were coated with TA (pH = 8) and copper ions to obtain DFMTC NPs. The final step was the preparation of DFMTCH NPs by modifying HA as the shielding layer of DFMTC NPs. Furthermore, based on scanning electron microscopy (SEM) and transmission electron microscopy (TEM) images, it could be observed that MIL-100 NPs and DFMTCH NPs all displayed a uniform spherical morphology (Fig. 2B, C, S1). Compared with MIL-100 NPs, the morphology of DFMTCH NPs was not affected by DOX and DSF, and the dispersibility of DFMTCH NPs was significantly improved after HA modification. Energy dispersive spectroscopy (EDS) spectra demonstrated the presence of Fe, Cu, and S elements in DFMTCH NPs with a uniform distribution, thereby confirming the successful synthesis of DFMTCH NPs (Fig. 2D). Similarly, X-ray photoelectron spectroscopy (XPS) also corroborated that the DFMTCH NPs were composed of Fe, Cu, C, N, O, S, and other elements (Fig. 2E). Moreover, we used XPS to analyze the valence states of iron and copper in DFMTCH NPs (Figs. S2 and 3). The results showed that the Fe element in DFMTCH NPs was composed of Fe^{3+} and Fe^{2+}, and the binding energy peaks at 711.6 eV (Fe 2p3/2) and 725.4 eV (Fe 2p1/2) confirmed the existence of Fe^{3+}, binding energy peaks at 714.0 and 717.7 eV confirm the presence of Fe^{2+} (Fig. S2). Similarly, the Cu 2p XPS spectrum of

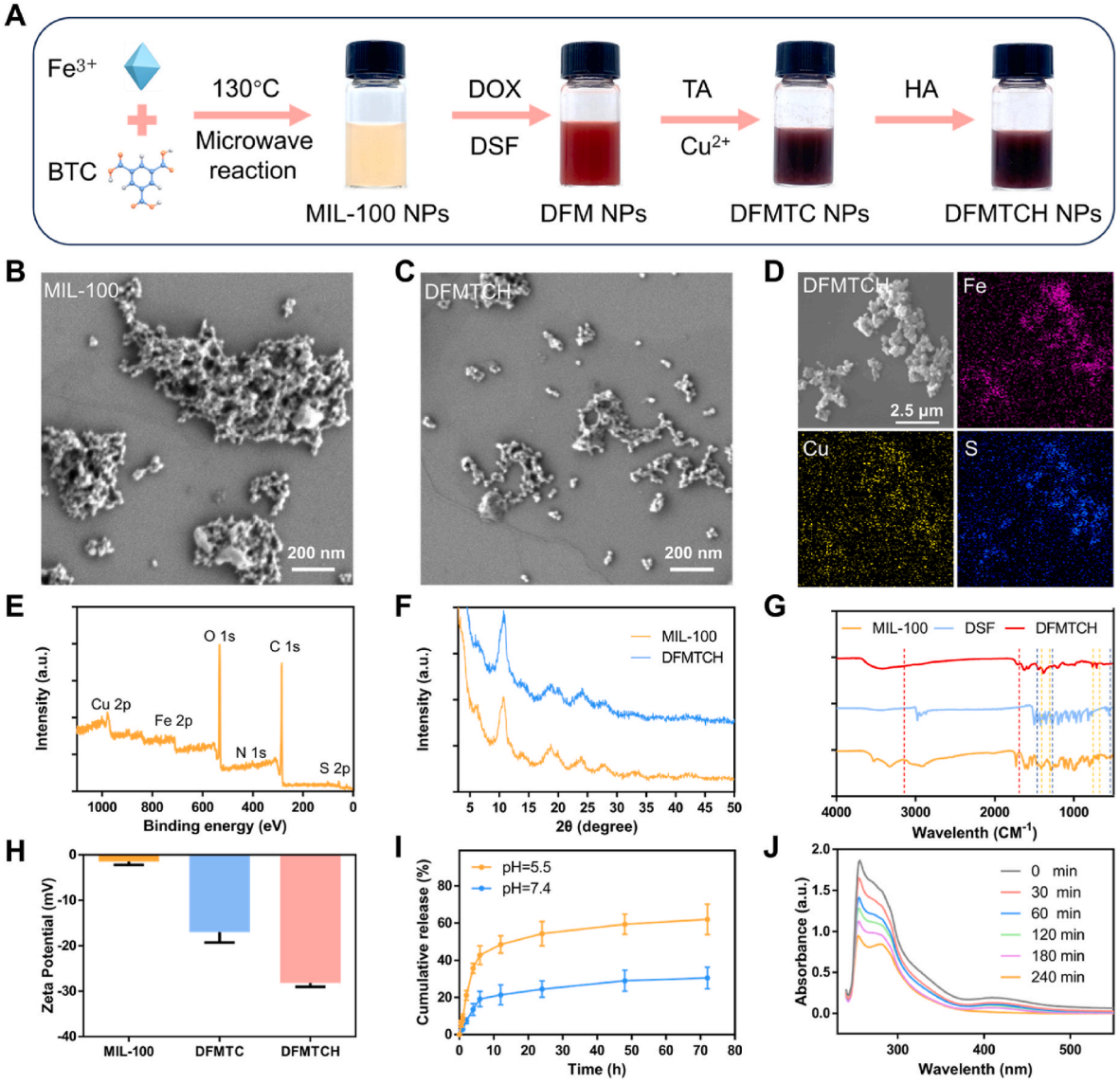

Fig. 2. Synthesis and characterization of nanoparticles. (A) Preparation process of DFMTCH NPs. SEM images of (B) MIL-100 NPs (C) DFMTCH NPs. (D) Element map for DFMTCH NPs. (E) XPS spectra of DFMTCH NPs. (F) XRD patterns. (G) FTIR spectra. (H) Zeta potential (n = 3). (I) Accumulative DOX release of DFMTCH NPs in PBS (n = 3). (J) UV–VIS curves of copper ethylthiocarbamate (CuET) formed after DFMTCH NPs were immersed in PBS (pH = 6.5) at different time intervals.

DFMTCH NPs showed a binding energy peak at 943.0 eV (2p3/2), confirming the presence of Cu^{2+} (Fig. S3). Furthermore, the total iron content in DFMTCH NPs was 6.25 ± 1.02 % and the total copper content was 2.63 ± 0.41 % by inductively coupled plasma mass spectrometry (ICP-MS) analysis (Table S1). It was noteworthy that the X-ray diffraction (XRD) results showed that the curve of DFMTCH NPs was similar to that of MIL-100 NPs, indicating that the loading of drugs DOX and DSF, along with the coating of Cu-TA and HA did not result in the destruction of the MOF structure (Fig. 2F). Fourier transform infrared spectroscopy (FTIR) spectra were utilized for the assessment of whether the DSF and DOX were successfully incorporated into DFMTCH NPs (Fig. 2G). MIL-100 NPs were identified by specific absorption bands, including ν (C-H), which was observed at 760 cm^{-1} and 711 cm^{-1}, as well as δ (O-H) and ν (O-C-O), which were observed at 1446 cm^{-1} and 1380 cm^{-1}. The characteristic absorption of DSF at 543 cm^{-1}, 1315 cm^{-1}, and 1498 cm^{-1} were attributed to the tensile vibrations of S-S, C=S, and C-N-C, respectively. The tensile vibration absorption of C=O (1693 cm^{-1}) and O-H (3160 cm^{-1}) were the characteristic absorption peak of DOX and TA. The presence of the aforementioned characteristic absorption peaks of DFMTCH NPs served to confirm the coexistence of DSF, DOX, and MIL-100 NPs. In addition, the fluorescence spectra of MIL-100, free DOX, DFMTC NPs and DFMTCH NPs were examined by fluorescence spectrometer. The results showed that a characteristic peak similar to that of DOX could be observed at 480 nm for both DFMTC NPs and DFMTCH NPs, which proved the successful loading of DOX (Fig. S4). Similarly, according to UV–VIS spectra, DFMTCH NPs showed characteristic peaks of DSF and DOX at 255 nm and 480 nm, which also verified the successful loading of DOX and DSF into the nanoparticles (Fig. S5). Additionally, based on the UV–VIS standard curve of DOX, we obtained the drug loading efficiency (DLE) and drug loading content (DLC) of DOX in DFM NPs. The weight ratio of MIL-100 NPs to DOX was chosen as 1:0.5 based on a DLE of 89.59 ± 1.04 % and a DLC of 30.97 ± 0.53 % (Table S2). In DFMTCH NPs, the loading rate of DOX was 17.53 ± 1.04 % (Table S3). Similarly, the ratio of MIL-100 NPs to DSF was determined to be 1:0.25, with a DLE of 56.27 ± 6.67 % and a DLC of 13.23 ± 1.47 % (Table S4). All the results showed that MIL-100 NPs were successfully synthesized and two drugs were successfully loaded for the next test.

The zeta potentials of MIL-100 NPs, DFMTC NPs and DFMTCH NPs were measured to be −1.29 mV, −13.25 mV and −28.10 mV, respectively (Fig. 2H). Compared with DFMTC NPs and DFMTCH NPs showed a lower zeta potential, indicating that HA was successfully coated on the surface of nanoparticles. The extremely negative zeta potential allowed the nanoparticles to remain stable without aggregating for long periods [24]. The evaluation using dynamic light scattering (DLS) revealed that the mean diameters of MIL-100 NPs, DFM NPs, and DFMTCH NPs were 97.5 nm, 112 nm, and 157.4 nm, respectively (Fig. S6). Furthermore, the stability of DFMTCH NPs was examined in deionized water, PBS, and 10 % FBS (Figs. S7–S9). The particle size of DFMTCH NPs remained stable after being incubated in deionized water, PBS, or DMEM for 72 h, which indicated that DFMTCH NPs were stable against salt ions and proteins, making them suitable for *in vivo* use. Moreover, the release of drugs from DFMTCH NPs was evaluated at pH 7.4 and 5.5, which simulated physiological and tumor microenvironments, respectively. As illustrated in Fig. 2I, a lower pH resulted in a higher release of DOX from DFMTCH NPs. Consequently, DFMTCH NPs exhibited pH-responsive drug release patterns in tumors with acidic microenvironments, which enhanced *in vivo* delivery of anti-tumor drugs and minimized abrupt release during somatic circulation. Furthermore, the co-released DSF and Cu^{2+} in DFMTCH NPs underwent a rapid reaction with each other, resulting in the generation of highly toxic CuET. This compound exhibited characteristic absorption peaks at 265 and 425 nm, and exhibited a time-dependent release pattern in weakly acidic conditions (Fig. 2J). The evaluation of stability and drug release demonstrated the ability of DFMTCH NPs to provide controlled drug release in acidic tumor microenvironments, in addition to the potential to maintain long-term drug circulation *in vivo*, which was critical for the development of anti-cancer nanocarriers with low toxicity and high efficacy.

2.2. Basic properties of DFMTCH NPs

DFMTCH NPs are rich in Fe^{3+} and Cu^{2+}, which can catalyze the Fenton/Fenton-like reaction, producing ·OH to achieve CDT, and having potential for cancer therapy (Fig. 3A). When the nanoparticles reached the tumor area, released Fe^{3+} and Cu^{2+} and activated the Fenton/like Fenton reaction, catalyzing the generation of ·OH from H_2O_2 [17]. Large amount of ·OH would further oxidize the cell membrane, protein molecules, and DNA of the tumor cells, thus triggering cell death [25]. To demonstrate CDT, MB was used as an indicator of ROS generation. DFMH NPs, DFMTH NPs, and DFMTCH NPs were co-incubated with MB for 30 min. The absorbance of MB decreased to varying degrees, indicating that the DFMTCH NPs were capable of generating ROS (Fig. 3B). We observed that the introduction of Cu^{2+} significantly enhanced ROS generation, which was attributed to the higher rate of the Cu^{2+}-catalyzed Fenton-like reaction in weakly acidic or neutral media compared to that of the Fe^{3+}-catalyzed Fenton reaction [26]. It was important to note that the introduction of TA also increased ROS production, which was in line with previous studies [27]. Additionally, the degradation of MB by DFMTCH NPs confirmed a concentration-dependent behavior (Fig. 3C). The intracellular antioxidant GSH protects cells from damage caused by ROS while assisting in maintaining the REDOX balance of cells [28]. However, the abundant Fe^{3+} and Cu^{2+} in DFMTCH NPs could deplete GSH by undergoing REDOX reactions. GSH reacted with DTNB to form a yellow product with a distinct adsorption peak at 410 nm, therefore, DTNB was chosen to measure GSH levels [29]. The results displayed that the introduction of Cu^{2+} and TA also significantly increased the depletion of GSH, which was consistent with the results of the ROS generation experiment (Fig. 3D). Furthermore, the capacity for GSH consumption was found to be significantly dose-dependent (Fig. 3E). The aforementioned results demonstrated that DFMTCH NPs possessed robust ROS generation and GSH depletion capabilities, enabling efficient CDT on CT-26 cells.

Moreover, the coordination of iron to TA in MIL-100 NPs enhanced their light absorption capacity in the near-infrared region, resulting in efficient PTT. When compared to MIL-100 NPs, DFMTCH NPs exhibited an enhanced absorption capacity at 808 nm, as evidenced by a change in color to black (Fig. 3F, S10). Fig. 2G, H illustrated the effect of laser power and DFMTCH NPs concentration on the photothermal effect, demonstrating a direct correlation between the photothermal effect and laser power intensity or DFMTCH NPs concentration. At the appropriate concentration and laser power intensity, the temperature of the aqueous solution containing DFMTCH NPs increased significantly, which indicated that the DFMTCH NPs were able to effectively ablate tumor cells through the photothermal effect (Fig. S11). The component of DFMTCH NPs with a photothermal conversion effect is Fe-TA [30]. In some recent studies, we found that Fe-TA based nanoparticles had good photothermal conversion ability [30,31]. The photothermal conversion ability of DFMTCH NPs and Fe-TA under the same conditions was compared, and the results showed that both DFMTCH NPs and Fe-TA had good photothermal conversion ability (Fig. S12). In addition, by comparing the heating and cooling curves of DFMTCH NPs with water, the photothermal conversion efficiency of DFMTCH NPs was calculated to be 32.17 % (Fig. S13) [32,33]. In a previous study, Fe-TA based nanoparticles had a photothermal efficiency of 29.8 %, which was similar to our results [31]. Additionally, the photothermal stability of DFMTCH NPs was demonstrated in Fig. 2I. The maximum temperatures of the five heating/cooling cycles did not change significantly, indicating that the DFMTCH NPs confirmed photothermal stability throughout the experimental evaluation.

2.3. Therapeutic efficacy of DFMTCH in living cells

The cell uptake efficiency of DFMTCH NPs was evaluated using

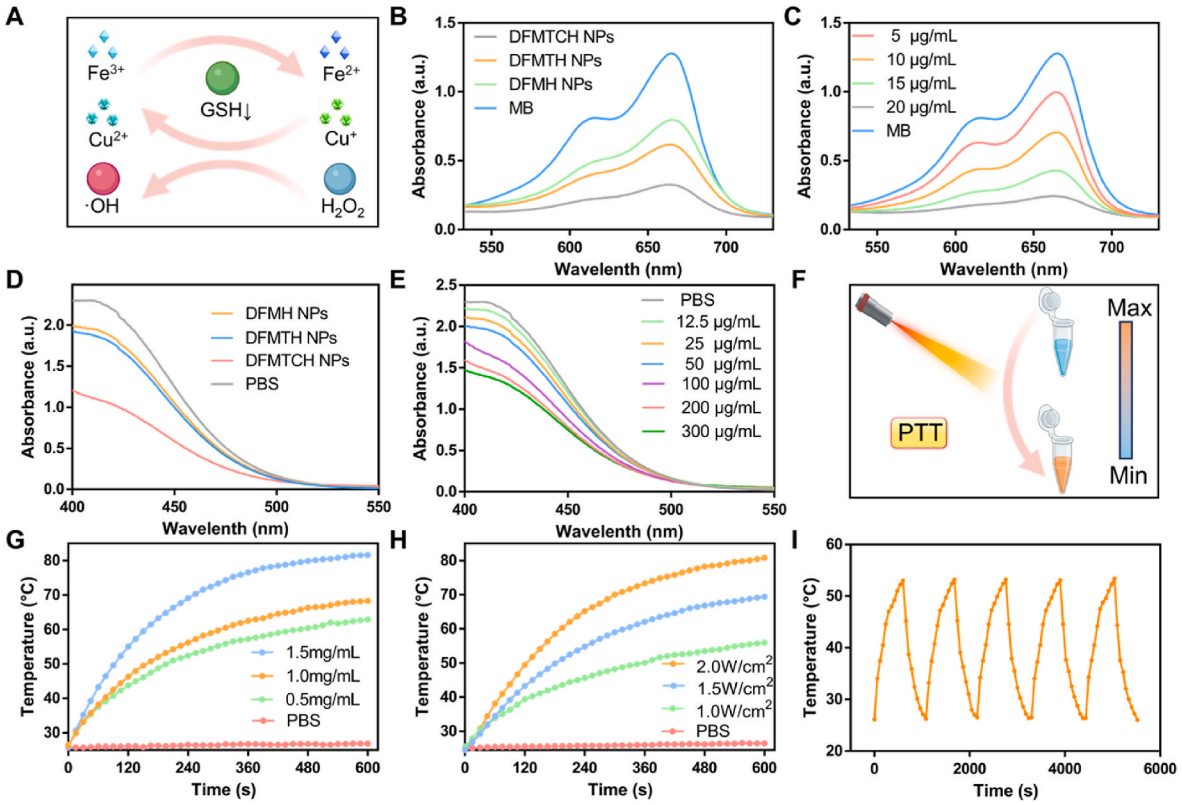

Fig. 3. Basic properties of DFMTCH NPs. (A) Fenton/Fenton-like reactions induced by DFMTCH NPs. (B) ·OH generation of nanoparticles using the MB assay. (C) ·OH generation at different concentrations of DFMTCH NPs using the MB assay. (D) GSH depleting ability detected with DTNB probe. (E) GSH depleting ability at different concentrations of DFMTCH NPs detected with DTNB probe. (F) Photothermal conversion capacity of DFMTCH NPs. (G) Photothermal curves of DFMTCH NPs at different concentration (1.5 W/cm^2; 0.5, 1.0, and 1.5 mg/mL). (H) Photothermal curves of DFMTCH NPs at different power (0.75 mg/mL; 1.0, 1.5, and 2 W/cm^2). (I) Temperature curves of DFMTCH NPs under the laser to investigate the photothermal stability of DFMTCH NPs solution.

fluorescence microscopy after co-incubating with CT-26 cells for different durations (2, 4, and 8 h, respectively). As illustrated in Fig. 4A showed that DOX red fluorescence was observed in CT-26 cells, and the intensity of DOX red fluorescence increased with time. Therefore, DFMTCH NPs could be internalized into CT-26 cells, and the cellular uptake of DFMTCH NPs was time-dependent, which might contribute to the potent anti-tumor effect of DFMTCH NPs.

In addition, MTT assay was performed on CT-26 cells to determine the cytotoxicity of the DFMTCH NPs under different conditions (Fig. 4B). After 24 h of incubation, free DOX established superior anti-tumor efficiency than DMTCH NPs at the same drug concentration, which might be attributed to the slow release of DOX in the DFMTCH NPs. In comparison to the FMTCH NPs group, the free DSF group exhibited lower cytotoxicity, this difference was attributed to the release of Cu^{2+} from FMTCH NPs into the tumor cells, which bounded with DSF to produce CuET, this reaction greatly enhanced the anti-tumor effect of DFMTCH NPs. Moreover, compared with free DOX free DSF, and FMTCH NPs, DFMTCH NPs demonstrated significant tumor cell killing ability, which was attributed to its loading with both DOX and DSF, as well as its high concentration of Fe^{3+} and Cu^{2+}, producing a large amount of ROS by Fenton/Fenton-like reaction, and thereby improving the therapeutic effect. The DFMTCH NPs + Laser group demonstrated the strongest anti-tumor efficiency, further supporting the effectiveness of photothermal therapy of DFMTCH NPs. It was noteworthy that, the biocompatibility of MIL-100 NPs, TA (pH = 8), and HA on-L929 cells was investigated using the MTT method. The results proved that even at a dose of 40 μg/mL, the above drugs did not produce significant deleterious effects on L929 cells (Fig. S14). To evaluate the distribution of live and dead cells visually, we stained the cells with AM and PI after 24 h of co-incubation with various preparations (Fig. 4C). Live cells fluoresced green, while dead cells fluoresced red. As expected, DFMTCH NPs induced massive cell death in CT-26 cells, while the DFMTCH NPs + Laser group showed the strongest anti-tumor effect. Similarly, the flow cytometry of live/dead cell staining showed the same results, which the DFMTCH group showed the strongest antitumor activity compared with the DFMTCH + Laser group (Fig. S15). All of these results suggested that combining chemotherapy, CDT, and PTT exhibited greater antitumor potential than any single treatment, and was expected to achieve efficient antitumor effects *in vivo*.

The pathological phenomenon of cancer metastasis often involves the process of cell migration [34]. The wound healing assay is a simple and efficient *in vitro* method to study cell migration, mimicking the process *in vivo* to some extent [35]. To determine the function of DFMTCH NPs in CT-26 cell migration and invasion, cells were treated with PBS, MIL-100 NPs, free DOX + DSF, and DFMTCH NPs, respectively. The cell healing rate in the DFMTCH NPs group was significantly lower than that in the other groups, indicating that DFMTCH NPs could reduce the migration ability of CT-26 cells (Fig. 4D and E). Additionally, a Transwell migration assay was performed to determine the migratory capacity of CT-26 cells after DFMTCH NPs treatment (Fig. 4F and G). The number of migrating cells after 24 h of exposure to DFMTCH NPs was significantly lower than in the other groups, which significantly inhibited the proliferation and migration ability of CT-26 cells. Furthermore, the colony formation assay was used to determine the proliferation ability of CT-26 cells (Fig. 4H and I). The colonies formed by CT-26 cells were significantly reduced in the DFMTCH NPs group compared with the control, MIL-100 NPs and free DOX + DSF groups, indicating that DFMTCH NPs affected the proliferation of CT-26 cells and significantly inhibited the colony formation ability. In addition, EdU experiments were performed to estimate the antiproliferative

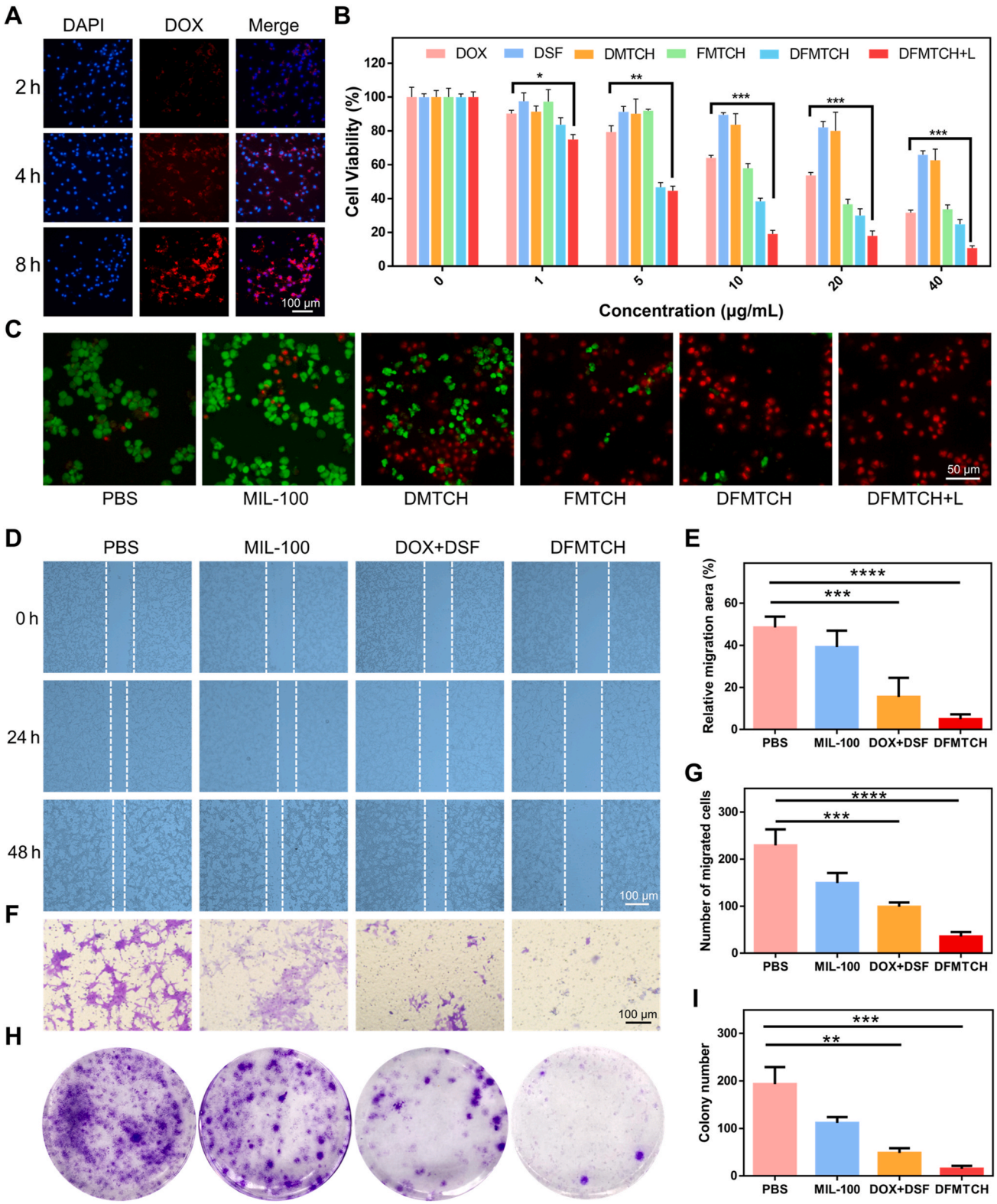

Fig. 4. Therapeutic efficacy of DFMTCH NPs *in vitro*. (A) Fluorescence imaging of CT-26 cells incubated with DFMTCH NPs at different time points. (B) Cell viability following nanoparticles or drugs incubation for 24 h at various concentrations (n = 3). Free drug concentrations were calculated from the drug-loaded equivalents of the DFMTCH NPs, with free DOX concentrations of 0, 0.2, 1, 2, 4, and 8 μg/mL, and DSF concentrations of 0, 0.1, 0.5, 1, 2, and 4 μg/mL, respectively. The concentrations of Fe and Cu were calculated from the results of ICP experiments, where the concentrations of Fe were 0, 0.06, 0.3, 0.6, 1.2, and 2.4 μg/mL, and the concentrations of Cu were 0, 0.03, 0.15, 0.3, 0.6, and 1.2 μg/mL. (C) Live/dead cell staining pictures of CT-26 cells under various conditions. (D) The wound healing assays in CT-26 cells under various interventions. (E) Quantification of the wound healing assays (n = 3). (F) Transwell migration assays in CT-26 cells under various interventions. (G) Quantification of Transwell migration assays (n = 3). (H) Representative pictures and quantification of clonogenic assays for CT-26 cells under the indicated treatment. (I) Quantification of clonogenic assays (n = 3). Statistical significance was set as follows: *p < 0.05, **p < 0.01, ***p < 0.001, ****p < 0.0001.

significance of DFMTCH NPs on CT-26 cells. The control group showed an intense green fluorescence representing proliferating cells, and the DFMTCH NPs-treated CT-26 cells exhibited the weakest green fluorescence, indicating an inhibitory effect on cell proliferation (Fig. S16). Overall, DFMTCH NPs were multifunctional drug-carrying nanoparticles that exhibited potent anti-tumor effects by combining chemotherapy, CDT, and PTT. Meanwhile, DFMTCH NPs effectively inhibited the proliferation and migration of CT-26 cells.

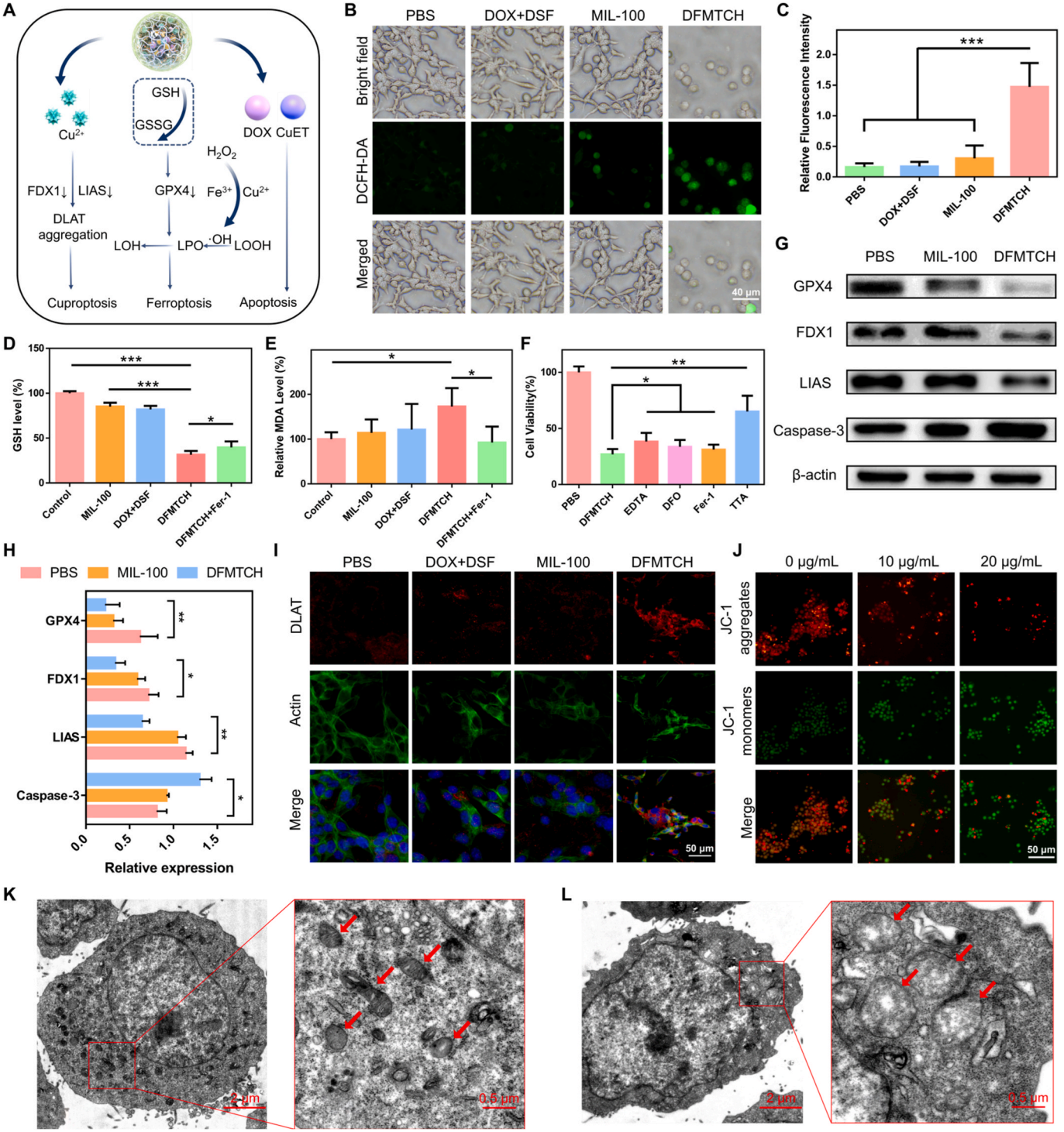

Fig. 5. Mechanism of DFMTCH NPs induced cell death. (A) The proposed schematic diagram of DFMTCH NPs-induced cuproptosis/ferroptosis/apoptosis. (B) Fluorescence pictures and (C) Fluorescence intensity evaluation of ROS formation in CT-26 cells (n = 3). Evaluation of the intracellular (D) GSH contents (n = 3) and (E) MDA in CT-26 cells upon distinct treatments (n = 3). (F) CT-26 cells' viabilities following a 24 h exposure to DFMTCH NPs alone or in combination with various suppressants (n = 3). (G, H) Western blot analysis on the expressions of GPX4, FDX1, LIAS, and caspase-3. (I) DLAT immunofluorescence images of cells in different groups. (J) Mitochondrial membrane potentials of CT-26 cells after different treatments. (K, L) Bio-TEM photographs of CT-26 cells subjected to (K) PBS and (L) DFMTCH NPs, red arrows indicated mitochondria. Statistical significance was set as follows: *p < 0.05, **p < 0.01, ***p < 0.001. (For interpretation of the references to color in this figure legend, the reader is referred to the Web version of this article.)

2.4. Mechanism of DFMTCH NPs induced cell death

Inspired by the *in vitro* anti-tumor efficacy of DFMTCH NPs, we sought to unravel antitumor mechanism of DFMTCH NPs. Fig. 5A depicted that DFMTCH NPs treat tumors by disrupting intracellular redox and Cu/Fe metabolism and synergizing with cuproptosis, ferroptosis, and apoptosis. The Fenton reaction process has been confirmed to produce ·OH in the tumor microenvironment [14]. These radicals react preferentially with tumor cell membranes, leading to lipid peroxidation and ferroptosis [36]. Intracellular iron accumulation is a prerequisite for the intracellular the Fenton reaction [37]. To verify the accumulation of iron in the cells, we employed the FerroOrange fluorescence probe to detect CT-26 cells after different treatments. The probe demonstrated an irreversible reaction with Fe^{2+} to form orange fluorescence products. As illustrated in Fig. S17, the DFMTCH NPs group exhibited a more pronounced orange fluorescence compared to the other groups following the co-incubation of the drug or nanoparticles with CT-26 cells for 4 h. These findings confirmed the release of Fe^{2+} of DFMTCH NPs *in vitro*, further verifying the effective accumulation of Fe^{2+} in cells.

DCFHDA was used as an indicator to validate intracellular ROS levels. CT-26 cells treated in the DFMTCH NPs group exhibited stronger green fluorescence than the control group, indicating a substantial quantity of ROS production within CT-26 cells, which was attributed to the abundance of Fe^{3+} and Cu^{2+} in DFMTCH NPs (Fig. 5B and C). In addition, GSH, as the most important endogenous antioxidant, is closely associated with ferroptosis, cuproptosis, and apoptosis [38]. Therefore, intracellular GSH depletion induced by DFMTCH NPs was investigated using GSH kits. As expected, DFMTCH NPs could greatly clear GSH in CT-26 cells, which was thought to be due to the release of Fe^{3+} and Cu^{2+} after DFMTCH NPs enter the cell, producing a large amount of ROS that react with GSH (Fig. 5D). In addition, GSH consumption was reduced in CT-26 cells treated with the Fer-1 inhibitor, which might be because Fer-1 was a lipid ROS scavger, reducing intracellular ROS and increasing intracellular GSH content, thereby affecting the process of ferroptosis. Similarly, the ratio of GSH to GSSG began to be severely dysregulated in CT-26 cells treated with DFMTCH NPs, which was one of the evidences of ferroptosis occurring within the cells (Fig. S18). Consequently, upon entering the interior of CT-26 cells, DFMTCH NPs could not only produce a substantial amount of ROS, but also efficiently depleted GSH, providing evidence for ferroptosis.

Lipid peroxidation is one of the important characteristics of ferroptosis [39]. To confirm lipid peroxidation, we measured the content of MDA, the natural end product of lipid peroxidation, which indicates LPO levels in cells [40]. The cells treated with DFMTCH NPs exhibited higher MDA levels compared to the control group (Fig. 5E). However, co-treatment with Fer-1 resulted in significantly lower MDA levels, suggesting that Fer-1 blocked DFMTCH-induced ferroptosis in CT-26 cells. To detect LPO processes inside the cell, we used the BODIPY 581/591C11 fluorescent probe, which would change from red to green after passing through the intracellular LPO process, and the intracellular LPO process could be clarified by observing the intensity of red/green fluorescence (Fig. S19). Similar to the results of MDA assay, the results showed that CT-26 cells treated with DFMTCH NPs exhibited the strongest green fluorescence, which revealed that DFMTCH NPs could efficiently induce the intracellular LPO process and provided a reliable basis for ferroptosis. To more effectively illustrate the ferroptosis observed in cells exposed to DFMTCH NPs, we conducted cell viability rescue experiments to elucidate the mechanism of DFMTCH NPs-mediated cell death (Fig. 5F). Our findings verified that exposure to CT-26 cells from DFMTCH NPs could effectively reversed cell viability with EDTA, DFO, and Fer-1 (three inhibitors of ferroptosis), and these results clearly demonstrated DFMTCH NPs-induced ferroptosis by intracellular iron accumulation and lipid peroxidation.

In addition, the expression of proteins associated with ferroptosis was examined to detect changes at the molecular level. GPX4, a key regulator of ferroptosis, was significantly down-regulated in CT-26 cells treated with DFMTCH NPs, which might be attributed to the inactivation of GPX4 caused by the powerful GSH-depleting capacity of DFMTCH NPs (Fig. 5G and H). In summary, DFMTCH NPs depleted GSH in CT-26 cells and triggered the inactivation of GPX4, resulting in to ROS production and lipid peroxidation, which could be converted by ferroptosis inhibitors, thus providing evidence of ferroptosis.

DLAT is a key protein in the tricarboxylic acid cycle, Cu^{2+} can bind directly to DLAT, leading to DLAT aggregation and subsequent proteotoxic stress, which ultimately results in cuproptosis [41]. DLAT oligomerization was investigated by immunofluorescence imaging. Cells treated with PBS, MIL-100 NPs or free DOX/DSF showed negligible DLAT foci, whereas cells treated with DFMTCH NPs exhibited pronounced DLAT foci (Fig. 5I). The formation of foci was attributed to abnormal oligomerization of DLAT. Furthermore, DFMTCH NPs significantly reduced the expression of the FDX1 and LIAS (Fig. 5G and H), which played a crucial role in the regulation of cuproptosis, and their loss was another characteristic of cuproptosis. Additionally, cell viability rescue experiments demonstrated that TTA, a cuproptosis inhibitor, significantly reversed the cell viability of CT-26 cells exposed to DFMTCH NPs (Fig. 5F), which suggested that cuproptosis played a pivotal role in DFMTCH NPs-induced cell death.

Mitochondria are the convergence point for many lethal signal transduction pathways [42]. For instance, ferroptosis is accompanied by mitochondrial dysfunction, which is characterized by the loss of mitochondrial membrane potential (MMP), mitochondrial fragmentation, and mitochondrial shrinkage [43]. Cuproptosis is triggered by the aggregation of the mitochondrial lipid acylation protein DLAT [44,45]. DFMTCH NPs was detected using JC-1 as a fluorescent indicator, which emits red fluorescence in healthy mitochondria with high MMP, but tends to show green fluorescence in abnormal mitochondria with low MMP [46]. The cells treated with high concentration of DFMTCH NPs showed strong green fluorescence and weak red fluorescence, indicating severe mitochondrial damage (Fig. 5J). Moreover, biological transmission electron microscopy was used to observe the morphological changes of mitochondria before and after DFMTCH NPs treatment (Fig. 5K and L). The results showed that DFMTCH NPs caused significant mitochondrial damage, including a decrease in mitochondrial volume, disappearance of mitochondrial cristae, an increase in membrane density, and even mitochondrial swelling and cavitation.

As apoptosis is the primary mechanism through which DOX and CuET exert their anti-cancer effects [47,48], we hypothesized that DFMTCH NPs could also induce cell death. Caspase-3 is a protease present in the cytoplasm that plays an important role in programmed cell death, especially apoptosis [49]. We examined the expression level of the key apoptotic protein caspase-3. As expected, caspase-3 expression was upregulated in cells treated with DFMTCH NPs (Fig. 5G and H). We suggested that the ability of DFMTCH NPs to successfully induce apoptosis in CT-26 cells was due to efficient loading of the chemotherapeutic drug DOX and *in situ* intracellular generation of CuET. In conclusion, these results convincingly revealed that DFMTCH NPs could significantly induce synergistic cuproptosis/ferroptosis/apoptosis, achieving effective therapeutic effects.

2.5. Biodistribution in vivo and photoacoustic imaging

First, the photothermal imaging capability of DFMTCH NPs in CT-26 tumor-bearing mice were verified (Fig. 6A). After intravenous injection of DFMTCH NPs into CT-26 tumor-bearing mice 12 h, the tumor surface temperature of mice treated with DFMTCH NPs rapidly reached 56.2 °C under 808 nm laser irradiation with a power density of 1 W/cm^2, highlighting the excellent photothermal properties and thermal imaging capabilities of DFMTCH NPs *in vivo*, and also provided evidence that DFMTCH NPs could effectively accumulate tumor sites. The biological distribution of DFMTCH NPs also led to similar results (Fig. 6B and C). DFMTCH NPs was injected intravenously into CT-26 tumor-bearing mice, and the distribution of tumors in major organs and tumors *in vivo*

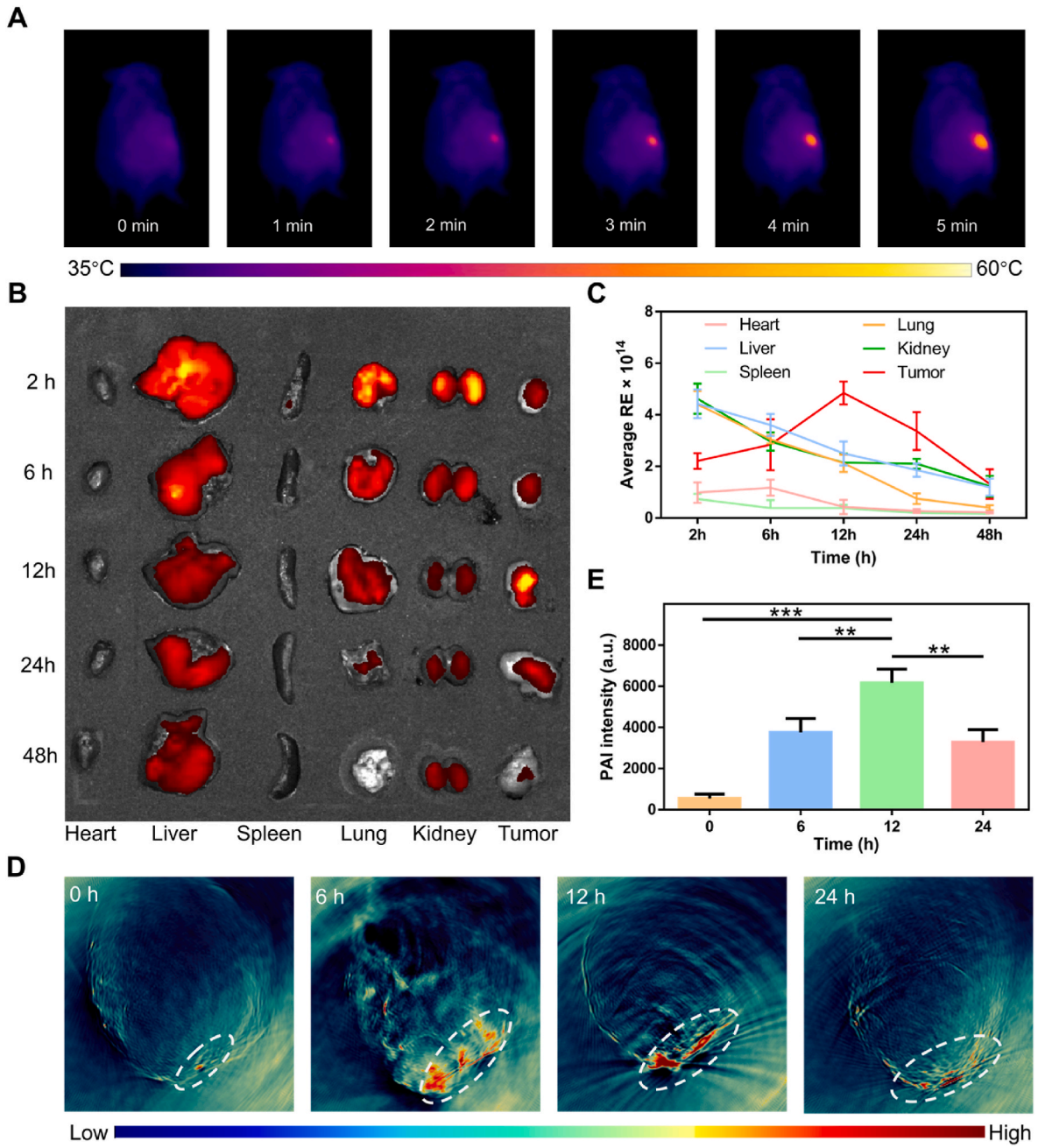

Fig. 6. Photothermal imaging, *in vivo* distribution and PAI of DFMTCH NPs. (A) Photothermal images of CT-26 Photothermal images of tumor-bearing mice treated with DFMTCH NPs under 808 nm laser irradiation (1.0 W/cm^2). (B, C) Biological distribution of DFMTCH NPs in major organs and tumors at different times (2, 6, 12, 24, and 48 h) after injection (n = 3). Representative (D) PAI images and (E) PAI intensity of DFMTCH NPs at different times (0, 6, 12, and 24 h), (n = 3). Statistical significance was set as follows: *p < 0.05, **p < 0.01, ***p < 0.001.

was observed at distinct time points by the NIR fluorescence imaging system. As illustrated in Fig. 6B and C, the intra-tumor DOX fluorescence gradually increased with time, reaching the highest level 12 h after injection. The tumors have the highest fluorescence intensity compared to major organs, which might be attributed to the EPR effect with an appropriate particle size of DFMTCH NPs.

Photoacoustic imaging (PAI) is a highly sensitive, non-invasive imaging method that can detect pressure waves caused by photoacoustic effects and is widely used in various tumor imaging protocols [50]. Since DFMTCH NP has a strong near-infrared absorbance, the photoacoustic signal was detected using an MSOT scanner. First, the photoacoustic signal of DFMTCH NPs increased gradually and linearly with the increase of DMTCH NP concentration (Fig. S20). The *in vivo* imaging capability of DFMTCH NPs in CT-26 tumor-bearing mice was further evaluated (Fig. 6D and E), the results showed that the PA signal in the tumor area was gradually enhanced and reached the maximum at 12 h after injection, which was similar to the conclusions drawn from the biological distribution in the body. And these results clearly confirmed the ability of DFMTCH NPs to accumulate at the tumor site.

2.6. Combined anti-cancer therapy in vivo

To investigate the combined anti-tumor effects of DFMTCH NPs *in vivo*, the *in vitro* therapeutic ability was detected (Fig. 7A). CT-26 tumor-bearing mice were randomly divided into 7 groups: PBS, MIL-100 NPs, free DOX, DMTCH NPs, FMTCH NPs, DFMTCH NPs, and DFMTCH NPs

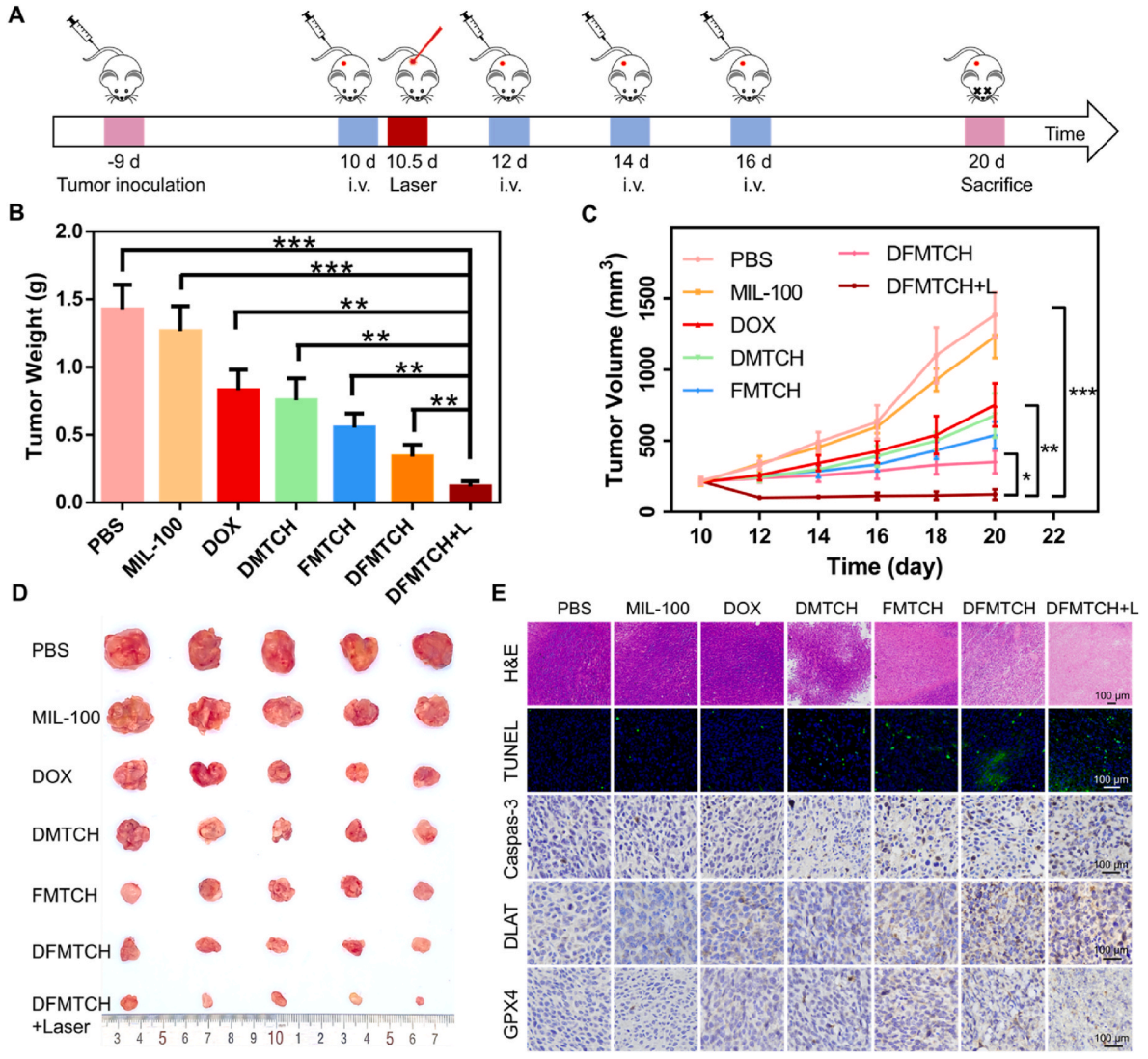

Fig. 7. Therapeutic effectiveness of DFMTCH NPs *in vivo*. (A) Schematic illustration of CT-26 tumor-bearing mice treated with different treatments. (B) The tumor weight of the mice in the different groups (n = 5). (C) The relative tumor volume curves of mice treated in different groups (n = 5). (D) Representative tumor photos of mice after the different treatments. (E) Pictures of tumors stained with H&E, TUNEL, Caspase-3, DLAT, and GPX4. Statistical significance was set as follows: *p < 0.05, **p < 0.01, ***p < 0.001.

+ Laser, and mice in each group were injected intravenously every 3 days. In the DFMTCH NPs + Laser group, the tumors were irradiated with an 808 nm laser at a power density of 1 W/cm^2 for 5 min. The efficacy of the treatment was demonstrated through the presentation of tumor images, tumor volume, and tumor weight (Fig. 7B–D). The tumor volume of MIL-100 NPs-treated mice showed a specific inhibition of tumor growth compared to the PBS group, which was due to the destruction of tumor cells by the Fenton/Fenton-like reaction (Fig. 7B and C). Furthermore, when DOX was loaded into MIL-100 NPs under the same conditions, the DMTCH NPs group exhibited superior tumor inhibition compared to the free DOX group, which might be attributed to the extended circulation time of DMTCH NPs and the accumulation of the EPR effect, thereby enhancing the utilization efficiency of DOX. The DFMTCH NPs + Laser group showed the highest level of tumor inhibition effect compared to the other treatment groups, which was due to the combined effects of chemotherapy, CDT, and PTT.

To confirm the therapeutic efficacy of DFMTCH NPs, we performed hematoxylin and eosin staining (H&E) of tumor tissues (Fig. 7E). We observed more nuclear fragments, eosinophilic red staining of the cytoplasm, and collagen fiber breakage in the intercellular material of tumor tissues in the DFMTCH NPs + Laser group. The synergistic benefits of chemotherapy, CDT, and PTT were more pronounced compared to single chemotherapy. All anti-tumor results indicated that the DFMTCH NPs + Laser group significantly inhibited tumor growth through the combination of chemotherapy, CDT, and PTT, and the combination treatment group was superior to the single treatment group.

The superior anti-tumor efficacy of DFMTCH NPs was also supported by terminal deoxynucleotidyl transferase-mediated dUTP nickel-end labelling (TUNEL) staining at the end of treatment (Fig. 7E). To gain insight into the *in vivo* anti-tumor mechanism of DFMTCH NPs, the expression of DLAT, GPX4, and caspase-3 in tumors were detected using immunohistochemical method (Fig. 7E). Consistent with the *in vitro* results, DFMTCH NPs-treated tumors exhibited the obvious DLAT aggregation, validating the presence of cuproptosis *in vivo*. Similarly, the key proteins for cuproptosis, FDX1 and LIAS, showed significant inactivation after treatment with DFMTCH NPs, providing evidence for cuproptosis (Fig. S21). Additionally, the DFMTCH NPs and DFMTCH NPs + Laser groups showed the most significant GPX4 downregulation and caspase-3 upregulation, indicating that DFMTCH NPs effectively inhibited tumor growth through cuproptosis/ferroptosis/apoptosis pathway (Fig. 7E).

Several methods were used to investigate the biosafety of DFMTCH NPs. First, the weight of CT-26 tumor-bearing mice in each group remained relatively stable during treatment (Fig. S22). This showed that the treatment process had little effect on the growth and health of the mice. The biocompatibility of DFMTCH NPs in the blood system through a hemolysis assay were investigated (Fig. S23). The hemolysis rates of DFMTCH NPs at concentrations ranging from 5 to 200 μg/mL were maintained at low levels, demonstrating excellent blood safety and acceptability for intravenous injection. In addition, blood was collected from mice in the DFMTCH NPs group on days 10, 15, and 20 for routine blood tests. The red blood cells, hemoglobin, white blood cells, and platelets were all within the normal range (Figs. S24–27). At the same time, we tested the liver and kidney functions of mice, including Alanine Aminotransferase (ALT), Aspartate Aminotransferase (AST) Blood Urea Nitrogen (BUN) and Creatinine (CREA), and the experimental results showed that the liver and kidney functions of mice were not significantly damaged (Figs. S28–31). In addition, histopathological examination of the main organs of mice in each group was performed using H&E staining to observe whether histological damage occurred (Fig. S32). Staining of organ sections from both the experimental and control groups revealed comparable histological structures, indicating that DFMTCH NPs treatment had low adverse effects on major organs in the short or long term. Therefore, the above results concluded that DFMTCH NPs had good biocompatibility and negligible side effects, making it an effective option for *in vivo* tumor therapy.

Consequently, DFMTCH NPs in the form of chemotherapy, CDT, and PTT combination therapy could markedly suppress tumor growth while exhibiting promise in driving apoptosis, ferroptosis, and cuproptosis in CRC therapy. In the past, CRC was often treated with a single chemotherapeutic approach, which had high side effects, poor efficacy, and easily triggered tumor resistance to apoptosis [51]. However, the DFMTCH NPs prepared in this study used a variety of highly effective therapeutic methods, including chemotherapy, CDT, and PTT, to achieve a comprehensive treatment of CRC and achieved good efficacy. Furthermore, in order to overcome apoptosis resistance in CRC, it is beneficial to induce non-apoptotic cell death, such as ferroptosis and cuproptosis in tumors [52]. The results of this study demonstrated that DFMTCH NPs could effectively induce tumor cells to undergo apoptosis, cuproptosis, and ferroptosis, thereby overcoming the resistance of tumors to chemotherapeutic agents to a certain extent. Moreover, DFMTCH NPs have an advantageous biosafety profile, with minimal side effects. Nevertheless, further studies are essential to comprehensively comprehend the potential of DFMTCH NPs in cancer treatment and to substantiate the efficacy and safety of this approach in clinical settings.

3. Conclusion

Given the limited efficacy of chemotherapy, DFMTCH NPs was endowed with the capacity for PTT, CDT, and chemotherapy, thereby achieving a markedly enhanced efficacy in combining multiple therapeutic modalities for the management of tumors. Furthermore, in order to circumvent the resistance of tumor cells to apoptosis induced by conventional chemotherapeutic agents, DFMTCH NP was attempted to simultaneously induce cuproptosis/ferroptosis/apoptosis in tumor cells. The accumulation of Fe^{3+}, the depletion of intracellular GSH, coupled with the enhanced production of ROS, resulted in the inactivation of GPX4, which collectively contributed to the effective induction of ferroptosis. Moreover, the presence of excess Cu^{2+} in DFMTCH NPs resulted in the induction of cuprotosis through the aggregation of DLAT. It was noteworthy that DFMTCH NPs showed favorable biosafety with minimal side effects *in vivo*. In conclusion, our findings demonstrated the potential of a synergistic approach combining PTT, CDT, and chemotherapy to induce intracellular cuproptosis and ferroptosis, as well as apoptosis, which offered a potential strategy for future integrated tumor therapy.

CRediT authorship contribution statement

Xiuzhang Yan: Writing – original draft, Data curation. **Heshi Liu:** Data curation. **Lei Guo:** Data curation. **Chang Liu:** Data curation. **Shichen Zhang:** Data curation. **Xue Wang:** Data curation. **Yixin Tang:** Data curation. **Rui Zhou:** Data curation. **Xin Jiang:** Data curation. **Erlei Wang:** Writing – review & editing. **Shuohui Gao:** Writing – review & editing. **Caina Xu:** Writing – review & editing.

Institutional review board statement

Not applicable.
Informed Consent Statement.
Not applicable.

Funding

The authors are thankful to the National Natural Science Foundation of China (52073278), the "Medical Science + X″ Cross-innovation Team of the Norman Bethune Health Science of Jilin University (2022JBGS10), the Natural Science Foundation of Jilin Province (YDZJ202201ZYTS118), the Education Department of Jilin Province (JJKH20231205KJ), and the Fundamental Research Funds for the Central Universities (2022-JCXK-09).

Declaration of competing interest

The authors declare that they have no known competing financial interests or personal relationships that could have appeared to influence the work reported in this paper.

Appendix A. Supplementary data

Supplementary data to this article can be found online at https://doi.org/10.1016/j.mtbio.2024.101427.

Data availability

No data was used for the research described in the article.

References

[1] R.L. Siegel, N.S. Wagle, A. Cercek, R.A. Smith, A. Jemal, Colorectal cancer statistics, 2023, CA A Cancer J. Clin. 73 (3) (2023) 233–254.
[2] L.H. Biller, D. Schrag, Diagnosis and treatment of metastatic colorectal cancer: a review, J. Am. Med. Assoc. 325 (7) (2021) 669–685.
[3] T. Sawicki, M. Ruszkowska, A. Danielewicz, E. Niedźwiedzka, T. Arłukowicz, K. E. Przybyłowicz, A review of colorectal cancer in terms of epidemiology, risk factors, development, symptoms and diagnosis, Cancers 13 (9) (2021) 2025.
[4] X. Wang, X. Zhong, Z. Liu, L. Cheng, Recent progress of chemodynamic therapy-induced combination cancer therapy, Nano Today 35 (2020) 100946.
[5] G. Gao, X. Sun, G. Liang, Nanoagent-promoted mild-temperature photothermal therapy for cancer treatment, Adv. Funct. Mater. 31 (25) (2021) 2100738.
[6] Z. Dong, K. Xue, A. Verma, J. Shi, Z. Wei, X. Xia, K. Wang, X. Zhang, Photothermal therapy: a novel potential treatment for prostate cancer, Biomater. Sci. 12 (10) (2024) 2480–2503.
[7] Y. Hu, Y. Zhou, K. Li, D. Zhou, Recent advances in near-infrared stimulated nanohybrid hydrogels for cancer photothermal therapy, Biomater. Sci. 12 (18) (2024) 4590–4606.
[8] H. Ye, J. Yan, C. Ge, F. Wu, J. Zhu, M. Yin, L. Xie, Z. Zhou, L. Yin, Tumoral/exosomal PD-L1 silencing reinforces mild photothermal therapy by relieving systemic and local immunosuppression, Chem. Eng. J. 483 (2024) 149093.
[9] L. Yang, Z. Zhao, B. Tian, M. Yang, Y. Dong, B. Zhou, S. Gai, Y. Xie, J. Lin, A singular plasmonic-thermoelectric hollow nanostructure inducing apoptosis and cuproptosis for catalytic cancer therapy, Nat. Commun. 15 (1) (2024) 7499.
[10] F. Liu, T. Yang, X. Chang, L. Chen, C. Cheng, X. Peng, H. Liu, Y. Zhang, X. Chen, Intelligent gold nanocluster for effective treatment of malignant tumor via tumor-specific photothermal–chemodynamic therapy with AIE guidance, Natl. Sci. Rev. 11 (5) (2024) nwae113.
[11] Y. Liu, P. Bhattarai, Z. Dai, X. Chen, Photothermal therapy and photoacoustic imaging via nanotheranostics in fighting cancer, Chem. Soc. Rev. 48 (7) (2019) 2053–2108.

[12] D. Tang, X. Chen, G. Kroemer, Cuproptosis: a copper-triggered modality of mitochondrial cell death, Cell Res. 32 (5) (2022) 417–418.
[13] Y. Wang, L. Zhang, F. Zhou, Cuproptosis: a new form of programmed cell death, Cell. Mol. Immunol. 19 (8) (2022) 867–868.
[14] H. Ranji-Burachaloo, P.A. Gurr, D.E. Dunstan, G.G. Qiao, Cancer treatment through nanoparticle-facilitated Fenton reaction, ACS Nano 12 (12) (2018) 11819–11837.
[15] J. Li, F. Cao, H.-l. Yin, Z.-j. Huang, Z.-t. Lin, N. Mao, B. Sun, G. Wang, Ferroptosis: past, present and future, Cell Death Dis. 11 (2) (2020) 88.
[16] X. Jiang, B.R. Stockwell, M. Conrad, Ferroptosis: mechanisms, biology and role in disease, Nat. Rev. Mol. Cell Biol. 22 (4) (2021) 266–282.
[17] M. Zhang, Y. Chen, Q. Wang, C. Li, C. Yuan, J. Lu, Y. Luo, X. Liu, Nanocatalytic theranostics with intracellular mutual promotion for ferroptosis and chemo-photothermal therapy, J. Colloid Interface Sci. 657 (2024) 619–631.
[18] Y.-J. He, X.-Y. Liu, L. Xing, X. Wan, X. Chang, H.-L. Jiang, Fenton reaction-independent ferroptosis therapy via glutathione and iron redox couple sequentially triggered lipid peroxide generator, Biomaterials 241 (2020) 119911.
[19] D.A. Nichela, A.M. Berkovic, M.R. Costante, M.P. Juliarena, F.S. García Einschlag, Nitrobenzene degradation in Fenton-like systems using Cu(II) as catalyst. Comparison between Cu(II)- and Fe(III)-based systems, Chem. Eng. J. 228 (2013) 1148–1157.
[20] P. Horcajada, S. Surblé, C. Serre, D.-Y. Hong, Y.-K. Seo, J.-S. Chang, J.-M. Grenèche, I. Margiolaki, G. Férey, Synthesis and catalytic properties of MIL-100 (Fe), an iron(iii) carboxylate with large pores, Chem. Commun. (27) (2007) 2820–2822.
[21] Y. Zhang, L. Lin, L. Liu, F. Liu, S. Sheng, H. Tian, X. Chen, Positive feedback nanoamplifier responded to tumor microenvironments for self-enhanced tumor imaging and therapy, Biomaterials 216 (2019) 119255.
[22] I.K. Smith, T.L. Vierheller, C.A. Thorne, Assay of glutathione reductase in crude tissue homogenates using 5,5′-dithiobis(2-nitrobenzoic acid), Anal. Biochem. 175 (2) (1988) 408–413.
[23] D. Yu, Y. Zha, Z. Zhong, Y. Ruan, Z. Li, L. Sun, S. Hou, Improved detection of reactive oxygen species by DCFH-DA: new insight into self-amplification of fluorescence signal by light irradiation, Sensor. Actuator. B Chem. 339 (2021) 129878.
[24] S. Honary, F. Zahir, Effect of zeta potential on the properties of nano-drug delivery systems - a review (Part 1), Trop. J. Pharmaceut. Res. 12 (2) (2013) 265–273.
[25] H. Han, J. Li, H.A. Santos, Recent advances in Fenton and Fenton-like reaction mediated nanoparticle in cancer therapy, Biomedical Technology 3 (2023) 40–51.
[26] X. Meng, X. Zhang, M. Liu, B. Cai, N. He, Z. Wang, Fenton reaction-based nanomedicine in cancer chemodynamic and synergistic therapy, Appl. Mater. Today 21 (2020) 100864.
[27] P.K.B. Nagesh, P. Chowdhury, E. Hatami, S. Jain, N. Dan, V.K. Kashyap, S. C. Chauhan, M. Jaggi, M.M. Yallapu, Tannic acid inhibits lipid metabolism and induce ROS in prostate cancer cells, Sci. Rep. 10 (1) (2020) 980.
[28] T. Liu, L. Sun, Y. Zhang, Y. Wang, J. Zheng, Imbalanced GSH/ROS and sequential cell death, J. Biochem. Mol. Toxicol. 36 (1) (2022) e22942.
[29] Y. Zhu, J. Wu, K. Wang, H. Xu, M. Qu, Z. Gao, L. Guo, J. Xie, Facile and sensitive measurement of GSH/GSSG in cells by surface-enhanced Raman spectroscopy, Talanta 224 (2021) 121852.
[30] Z. Jiang, Z. Jiang, Y. Jiang, Y. Cheng, Q. Yao, R. Chen, L. Kou, Fe-involved nanostructures act as photothermal transduction agents in cancer photothermal therapy, Colloids Surf. B Biointerfaces 228 (2023) 113438.
[31] W. Cui, S. Zhu, X. Pan, W. Zhang, T. Wang, Gold(III) porphyrin-metal-polyphenolic nanocomplexes: breaking intracellular redox environment for enhancing mild-temperature photothermal therapy, ACS Appl. Mater. Interfaces 16 (24) (2024) 30810–30818.
[32] Q. Tian, F. Jiang, R. Zou, Q. Liu, Z. Chen, M. Zhu, S. Yang, J. Wang, J. Wang, J. Hu, Hydrophilic Cu9S5 nanocrystals: a photothermal agent with a 25.7% heat conversion efficiency for photothermal ablation of cancer cells in vivo, ACS Nano 5 (12) (2011) 9761–9771.
[33] B. Wang, J.-H. Wang, Q. Liu, H. Huang, M. Chen, K. Li, C. Li, X.-F. Yu, P.K. Chu, Rose-bengal-conjugated gold nanorods for in vivo photodynamic and photothermal oral cancer therapies, Biomaterials 35 (6) (2014) 1954–1966.
[34] P. Friedl, D. Gilmour, Collective cell migration in morphogenesis, regeneration and cancer, Nat. Rev. Mol. Cell Biol. 10 (7) (2009) 445–457.
[35] A. Grada, M. Otero-Vinas, F. Prieto-Castrillo, Z. Obagi, V. Falanga, Research techniques made simple: analysis of collective cell migration using the wound healing assay, J. Invest. Dermatol. 137 (2) (2017) e11–e16.
[36] J.Y. Cao, S.J. Dixon, Mechanisms of ferroptosis, Cell. Mol. Life Sci. 73 (11) (2016) 2195–2209.
[37] X. Qian, J. Zhang, Z. Gu, Y. Chen, Nanocatalysts-augmented Fenton chemical reaction for nanocatalytic tumor therapy, Biomaterials 211 (2019) 1–13.
[38] N. Liu, M. Chen, Crosstalk between ferroptosis and cuproptosis: from mechanism to potential clinical application, Biomed. Pharmacother. 171 (2024) 116115.
[39] F. Ursini, M. Maiorino, Lipid peroxidation and ferroptosis: the role of GSH and GPx4, Free Radic. Biol. Med. 152 (2020) 175–185.
[40] Z. Feng, W. Hu, L.J. Marnett, M.-s. Tang, Malondialdehyde, a major endogenous lipid peroxidation product, sensitizes human cells to UV- and BPDE-induced killing and mutagenesis through inhibition of nucleotide excision repair, Mutation Research/Fundamental and Molecular Mechanisms of Mutagenesis 601 (1) (2006) 125–136.
[41] L. Chen, J. Min, F. Wang, Copper homeostasis and cuproptosis in health and disease, Signal Transduct. Targeted Ther. 7 (1) (2022) 378.
[42] H. Vakifahmetoglu-Norberg, A.T. Ouchida, E. Norberg, The role of mitochondria in metabolism and cell death, Biochem. Biophys. Res. Commun. 482 (3) (2017) 426–431.
[43] M. Gao, J. Yi, J. Zhu, A.M. Minikes, P. Monian, C.B. Thompson, X. Jiang, Role of mitochondria in ferroptosis, Mol. Cell 73 (2) (2019) 354–363.e3.
[44] D. Tang, X. Chen, R. Kang, G. Kroemer, Ferroptosis: molecular mechanisms and health implications, Cell Res. 31 (2) (2021) 107–125.
[45] J. Xie, Y. Yang, Y. Gao, J. He, Cuproptosis: mechanisms and links with cancers, Mol. Cancer 22 (1) (2023) 46.
[46] A. Perelman, C. Wachtel, M. Cohen, S. Haupt, H. Shapiro, A. Tzur, JC-1: alternative excitation wavelengths facilitate mitochondrial membrane potential cytometry, Cell Death Dis. 3 (11) (2012).
[47] C. Chen, L. Lu, S. Yan, H. Yi, H. Yao, D. Wu, G. He, X. Tao, X. Deng, Autophagy and doxorubicin resistance in cancer, Anti Cancer Drugs 29 (1) (2018) 1–9.
[48] H. Li, J. Wang, C. Wu, L. Wang, Z.-S. Chen, W. Cui, The combination of disulfiram and copper for cancer treatment, Drug Discov. Today 25 (6) (2020) 1099–1108.
[49] M. Asadi, S. Taghizadeh, E. Kaviani, O. Vakili, M. Taheri-Anganeh, M. Tahamtan, A. Savardashtaki, Caspase-3: structure, function, and biotechnological aspects, Biotechnol. Appl. Biochem. 69 (4) (2022) 1633–1645.
[50] A.B.E. Attia, G. Balasundaram, M. Moothanchery, U.S. Dinish, R. Bi, V. Ntziachristos, M. Olivo, A review of clinical photoacoustic imaging: current and future trends, Photoacoustics 16 (2019) 100144.
[51] K. Van der Jeught, H.C. Xu, Y.J. Li, X.B. Lu, G. Ji, Drug resistance and new therapies in colorectal cancer, World J. Gastroenterol. 24 (34) (2018) 3834–3848.
[52] Y.-S. Lee, D.-H. Lee, H.A. Choudry, D.L. Bartlett, Y.J. Lee, Ferroptosis-induced endoplasmic reticulum stress: cross-talk between ferroptosis and apoptosis, Mol. Cancer Res. 16 (7) (2018) 1073–1076.